Expanded Limit Boundary Explicit Model Predictive Direct Speed Control for PMSMs

Mengyuan Zhao, Yanfei Cao, *Member, IEEE*, Chen Li, Zhiqiang Wang, *Member, IEEE*,
Tingna Shi, *Senior Member, IEEE*, and Changliang Xia, *Senior Member, IEEE*

***Abstract*—The utilization of the explicit model predictive (EMP) control method for direct speed control (DSC) of permanent magnet synchronous motors (PMSMs) achieves high-bandwidth speed control and excellent dynamic performance. However, the commonly used regular hexagonal current and voltage constraints restrict the motor's operational region, resulting in a narrow speed range and low load capacity. In addition, the conventional formula-based field-weakening method leads to undesirable allocation of *d*- and *q*-axis currents, reducing the degree of freedom in adjusting the motor's operating point. These drawbacks restrict the EMP-DSC method's application in the motor's extreme operation. Therefore, this article proposes an expanded limit boundary EMP-DSC method to realize cascade-free speed control with a wider speed range and higher load capacity. First, the proposed method constructs irregular hexagonal constraints, expanding the limit boundary of the motor's operational region in the i_{d}–i_{q} plane to broaden the speed and load ranges simultaneously. Then, based on these new constraints, an easily implementable optimal-trajectory field-weakening method is skillfully designed to optimize the current distribution, maintain the operating point near the optimal position, and improve field weakening performance. The proposed method enhances the competitiveness of EMP control in motor servo drive fields, and its feasibility is verified by experiments.**

***Index Terms*—Direct speed control (DSC), explicit model predictive (EMP) control, field weakening control, permanent magnet synchronous motor (PMSM).**

I. Introduction

PERMANENT magnet synchronous motors (PMSMs) are widely used in advanced servo drive fields, such as drones, electric vehicles, and robotics, by virtue of their high power density, good dynamic performance, and high reliability [1]. The growing demand for PMSMs' excellent dynamic and steady-state performance, expanded speed range, and enhanced load capacity is evident [2].

The classic PMSM speed control adopts the field-oriented control with a cascade structure, where the output of the speed outer loop serves as the reference input for the current inner loop [3], [4]. Over the years, cascaded control has been successfully used in various industrial applications. However, dual-loop cascaded control suffers from the following drawbacks: First, it is challenging to achieve multivariable coordinated optimal control due to the independent single-input and single-output controllers that separately control the speed, d-axis current, and q-axis current [5], [6]. Second, the constraint handling method of limiting the controller's output by upper and lower constraints usually leads to nonoptimal control quantities [7]. Third, the outer loop's bandwidth is generally much smaller than the inner loop, resulting in a limited dynamic performance of the speed [8], [9], [10]. To overcome these shortcomings of the traditional cascaded control, the cascade-free direct speed control (DSC) for PMSMs has become a hot topic in high-performance servo drives with high research value and practical significance [11].

Explicit model predictive (EMP) control has a powerful capability to handle constraints and exhibits excellent dynamic performance. It is highly suitable for cascade-free DSC of PMSMs because it allows for multivariable collaborative control using a single controller with adjustable weighting factors [7], [12]. EMP control was proposed by Bemporad in 2002 to reduce the online computational burden of the model predictive control (MPC), making it applicable to systems with higher control frequency [13]. Like MPC, EMP control constructs the optimal control problem based on the following three elements: the predictive model, the cost function, and constraints. The difference is that EMP control converts the optimal problem needed to be solved online at each control period in MPC into a multiparameter quadratic programming (MPQP) problem that can be presolved offline, significantly reducing the real-time calculation [14]. Specifically, the EMP algorithm divides the state space into a finite number of critical regions (CRs), calculating the optimal control law corresponding to each CR based on the Karush–Kuhn–Tucker conditions offline. The resulting optimal control law is an explicit and continuous piecewise affine function of the states. During real-time operation, it is only necessary to determine the CR to which the current

Manuscript received 3 June 2023; revised 23 November 2023; accepted 24 January 2024. Date of publication 29 January 2024; date of current version 20 March 2024. This work was supported in part by the Major Program of National Natural Science Foundation of China under Grant 51991384, in part by the Key Program of National Natural Science Foundation of China under Grant 52237003, and in part by Zhejiang Provincial "Pioneer" and "Leading Goose" R&D Program of China under Grant 2023C01178. Recommended for publication by Associate Editor J.B. He. *(Corresponding author: Tingna Shi.)*

Mengyuan Zhao, Yanfei Cao, Chen Li, and Tingna Shi are with the College of Electrical Engineering, Zhejiang University, Hangzhou 310027, China, and also with the Zhejiang University Advanced Electrical Equipment Innovation Center, Hangzhou 311107, China (e-mail: zhaomengyuan@zju.edu.cn; caoyanfei@zju.edu.cn; lichen_hz@zju.edu.cn; tnshi@zju.edu.cn).

Zhiqiang Wang is with the School of Electrical Engineering, Tiangong University, Tianjin 300387, China (e-mail: wangzhiqiang@tiangong.edu.cn).

Changliang Xia is with the School of Electrical Engineering, Tiangong University, Tianjin 300387, China, and also with the College of Electrical Engineering, Zhejiang University, Hangzhou 310027, China (e-mail: motor@tju.edu.cn).

Color versions of one or more figures in this article are available at https://doi.org/10.1109/TPEL.2024.3359283.

Digital Object Identifier 10.1109/TPEL.2024.3359283

states belong and invoke the corresponding optimal control law [15].

The existing EMP-DSC methods can achieve cascade-free speed control of PMSMs, providing effective current and voltage constraints and excellent dynamic performance [16], [17], [18], [19], [20]. The design process and core techniques for constructing a direct speed controller based on the EMP algorithm were first proposed in [16] to improve the dynamic performance of speed control. A Kalman filter was used to improve the load operation performance of the EMP-DSC system in [17], and an extended state observer (ESO) was used to enhance the disturbance rejection capability of the EMP-DSC system in [18]. To achieve field-weakening operation in EMP-DSC, Mynar et al. [19] provided a novel linearization method to preserve the critical information necessary for field-weakening operation. This method allows for the natural generation of negative i_{d} at high speeds. But this method somewhat reduces the i_{d}s control capability. A formula-based field-weakening method was presented in [20], in which the calculated reference value of i_{d} was augmented into the state vector, and the field weakening operation was realized by tracking control of i_{d}. Both the methods provided in [19] and [20] can achieve PMSM's cascade-free field-weakening operation and hold significant academic value. However, their research on extreme operations, such as high-speed and heavy-load is still in the early stages, with further optimization potential in terms of the speed range, load capacity, and allocation of d- and q-axis currents.

To this end, this article analyzes the limitations of the existing EMP-DSC method and then fully combines the mechanism of PMSM's field-weakening operation and the working principles of the EMP algorithm to propose an EMP-DSC method with an expanded limit boundary. The main contributions of the proposed method are summarized as follows.

1) The proposed method constructs irregular hexagonal current and voltage constraints. Use three constraint segments in the commonly used quadrant of the i_{d}–i_{q} plane to approximate the limit circle and use only one segment to replace the limit circle in the other quadrants, which broadens the reachable range of voltage and current vectors and expands the limit boundary of the motor's operational region. This simultaneously results in an expanded speed regulation range and increased load-carrying capacity in the entire speed range, including the constant torque and field weakening regions.
2) The proposed method designs an easily implementable optimal-trajectory field-weakening method with the help of the newly proposed voltage constraints. This method can comprehensively consider the dual requirements of speed tracking and load balancing while satisfying the dual constraints of current and voltage. The degree of freedom in adjusting the motor's operating point is increased, and the motor's actual operating point is maintained near the optimal position, optimizing the current allocation. On the one hand, the minimal i_{d} required to maintain the corresponding speed is utilized during high-speed light-load conditions. On the other hand, as the load changes, the d- and q-axis currents can adaptively adjust simultaneously to ensure that the i_{d}–i_{q} plane's current control trajectory follows the optimal trajectory, reaching the maximum load at the corresponding speed.

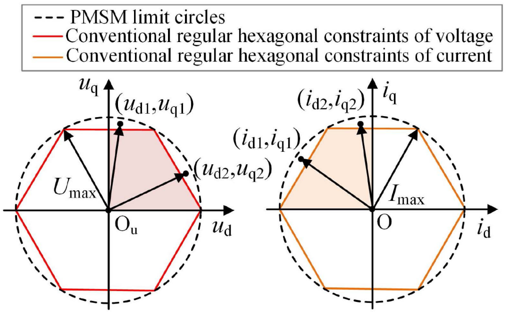

Fig. 1. Conventional regular hexagonal voltage and current constraints of the existing EMP-DSC methods.

The rest of this article is organized as follows. Section II analyzes the limitations of the existing EMP-DSC method. Section III proposes the new expanded limit boundary EMP-DSC method with irregular hexagon constraints and optimal-trajectory field-weakening method. Section IV provides performance analysis and stability proof of the proposed method. Section V develops the experiments. Finally, Section VI concludes this article.

II. PERFORMANCE ANALYSIS OF THE EXISTING EMP-DSC METHOD

A. Motor Operational Region Under the Conventional Regular Hexagon Constraints

During the operation of a PMSM, current and voltage constraints must be imposed due to limitations, such as inverter capacity and dc-bus voltage. The nonlinear equations for the current and voltage limit circles are as follows:

$$\begin{cases} i_{\mathrm{d}}^2 + i_{\mathrm{q}}^2 \le I_{\max}^2 \\ u_{\mathrm{d}}^2 + u_{\mathrm{q}}^2 \le U_{\max}^2 \end{cases} \tag{1}$$

where i_{d}, i_{q}, and u_{d}, u_{q} are the d- and q-axis stator currents and voltages, respectively; $I_{\max}$ and $U_{\max}$ are the maximum allowable current and voltage, respectively.

Because EMP algorithms require transforming nonlinear constraints into linear constraints, the existing EMP-DSC method commonly uses the inscribed regular hexagons to approximate the motor's current and voltage limit circles, as shown in Fig. 1. EMP control can directly impose constraints on states and their linear combinations, so the conventional regular hexagonal voltage and current constraints are, respectively, represented by a set of linear equations in matrix form

$$\boldsymbol{A}_{\mathrm{vc}} \begin{bmatrix} u_{\mathrm{d}}(k) \\ u_{\mathrm{q}}(k) \end{bmatrix} \le U_{\max} \cdot \boldsymbol{E}, \boldsymbol{A}_{\mathrm{ic}} \begin{bmatrix} i_{\mathrm{d}}(k) \\ i_{\mathrm{q}}(k) \end{bmatrix} \le I_{\max} \cdot \boldsymbol{E} \tag{2}$$

where $\boldsymbol{E} = [111111]^{\mathrm{T}}$; $\boldsymbol{A}_{\mathrm{vc}}$ and $\boldsymbol{A}_{\mathrm{ic}}$ are conventional voltage and current constraint matrices

$$\boldsymbol{A}_{\mathrm{vc}} = \boldsymbol{A}_{\mathrm{ic}} = \begin{bmatrix} 1 & 1 & 0 & 0 & -1 & -1 \\ \frac{1}{\sqrt{3}} & \frac{-1}{\sqrt{3}} & \frac{2}{\sqrt{3}} & \frac{-2}{\sqrt{3}} & \frac{1}{\sqrt{3}} & \frac{-1}{\sqrt{3}} \end{bmatrix}^{\mathrm{T}}. \tag{3}$$

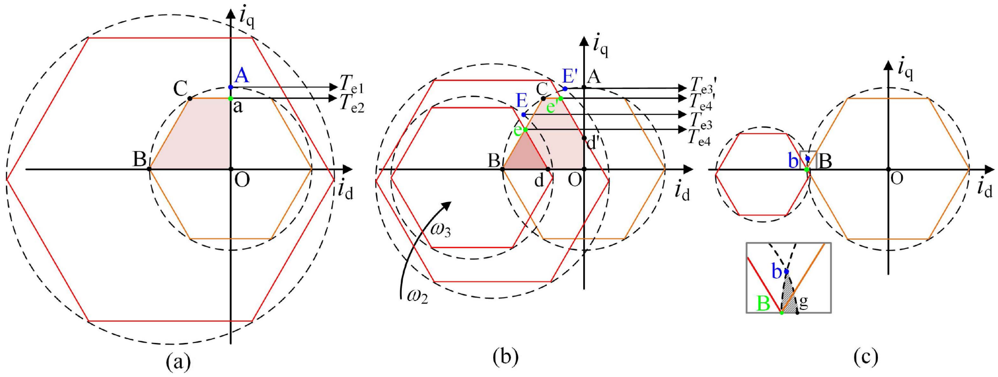

Fig. 2. PMSM's operational region and limit boundaries under the conventional regular hexagonal constraints. (a) ω_1. (b) ω_2 and ω_3. (c) ω_4.

It should be noted that EMP control directly imposes constraints on u_d and u_q so that the conventional regular hexagonal voltage constraint locates in the u_d–u_q plane and is an inscribed hexagon within the 2-level 3-phase voltage source inverter's (VSI's) linear modulation area, which is different from the $u_\alpha - u_\beta$ plane's regular hexagon formed by the VSI's basic voltage space vectors.

The traditional technique of approximating limit circles with inscribed regular hexagons to realize constraints' linearization unavoidably reduces the motor's operational region. Although this may not affect the motor's operation at low speeds and light loads, it severely limits its extreme operating capabilities, such as speed regulation range and load balancing range.

Specifically, the use of regular hexagonal constraints restricts the current and voltage vectors that can be used. For instance, the voltage vectors terminating at points (u_{d1}, u_{q1}) and (u_{d2}, u_{q2}), as well as the current vectors terminating at points (i_{d1}, i_{q1}) and (i_{d2}, i_{q2}) are no longer reachable. The voltage vectors' reachable region in the u_d–u_q plane's first quadrant (indicated by the pink shaded area in Fig. 1) and the current vectors' reachable region in the i_d–i_q plane's second quadrant (indicated by the orange shaded area in Fig. 1) are both reduced to 82.7% of that under the circular constraint.

As shown in Fig. 2, PMSM's voltage and current constraints are plotted in the i_d–i_q plane simultaneously. The current constraint remains fixed, while the voltage constraint shrinks as speed increases ($\omega_1 < \omega_2 < \omega_3 < \omega_4$, where ω is the mechanical angular speed). Because the stator resistive voltage drops are considered in this article, the voltage limit circle's center locates below the i_d-axis and moves as the speed changes [21], [22]. The constant torque locus is a line parallel to the i_d-axis ($T_{e4} < T_{e3} < T_{e2} < T_{e1}$, where T_e is the electromagnetic torque). The motor operation must satisfy both current and voltage constraints. Therefore, the motor's operational region is the overlapping area between the current and voltage constraint polygons in the i_d–i_q plane's second quadrant (indicated by the shaded region in Fig. 2), whose boundary is regarded as the motor's limit boundary.

In the following, limitations of regular hexagonal constraints of the existing EMP-DSC method are discussed under the following three typical operating conditions.

1) It can be seen from Fig. 2(a) that when the motor operates in the constant torque region (e.g., $\omega = \omega_1$), its operational region is the polygon O–a–C–B. Due to the $i_d = 0$ control strategy, the actual operational region is line segment O–a, shorter than the operational region line segment O–A under the circular constraints. Considering that i_q linearly increases as the load increases. The maximum achievable i_q under regular hexagonal constraints is $0.866 I_{\max}$ instead of the limit value $I_{\max}$ because the motor's operating point is limited to point a $(0, 0.866 I_{\max})$ and cannot reach point A (0, $I_{\max}$). Correspondingly, the maximum available torque in the constant torque region is limited to $T_{e2} = 0.866 k_t I_{\max}$ rather than the limit value $T_{e1} = k_t I_{\max}$ (where k_t is the torque constant). Hence, conventional regular hexagonal constraints reduce the motor's load-carrying capability in the constant torque region to 86.6% of that under the circular constraints.
2) It can be seen from Fig. 2(b) that when the motor operates in the field weakening region (e.g., $\omega = \omega_2$ and $\omega = \omega_3$), its operational regions are the polygon O–d'–e'–C–B and the triangle d–e–B, respectively. The intersection points between the voltage and current limit circles are E and E', while the intersection points between the voltage and current regular hexagonal constraints are e and e'. Therefore, even under the ideal condition, the use of regular hexagonal constraints reduces the maximum load-carrying capability from T_{e3}' (T_{e3}) corresponding to point E' (E) to T_{e4}' (T_{e4}) corresponding to point e' (e) when maintaining speed ω_2 (ω_3). Similarly, it can be deduced that conventional regular hexagonal constraints reduce the ideal maximum load-carrying capability at all speeds during the field weakening operation.
3) It can be seen from Fig. 2(c) that when $\omega = \omega_4$, the intersection between the current and voltage regular hexagonal constraints coincides with point B, which indicates that there is no feasible operational region except for point B under the existing method so that the motor reaches its maximum speed ω_4. However, the enlarged figure reveals that the intersection between the voltage and current limit circles is point b, so a feasible operational region, the polygon g–b–B, still exists under circular constraints. The motor can continue accelerating until the intersection point

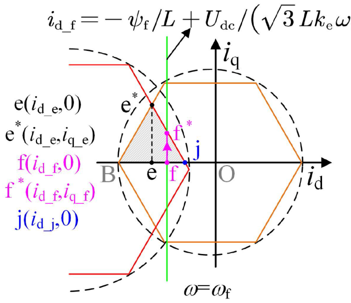

Fig. 3. Existing formula-based field-weakening method's current distribution.

b coincides with point B. Therefore, conventional regular hexagonal constraints reduce the motor's maximum achievable speed and narrow the speed range.

B. d/q-Axis Current Allocation Under the Conventional Formula-Based Field-Weakening Method

The existing EMP-DSC method employs a formula-based approach to achieve field-weakening operation. The calculation formula for the reference value of the field-weakening current i_{dref} is given by [20]

$$i_{\mathrm{dref}} = -\psi_{\mathrm{f}}/L + U_{\mathrm{dc}}/\left(\sqrt{3}Lk_{\mathrm{e}}\omega_{\mathrm{ref}}\right) \tag{4}$$

where ψ_{f}, L, U_{dc}, and k_{e} are the permanent magnet flux linkage, stator inductance, dc-bus voltage, and voltage constant, respectively.

The principle of the conventional formula-based field-weakening method can be inferred from (4) that when the back electromotive force reaches its limit, the motor maintains full-voltage high-speed operation by applying a negative i_{d} to weaken the magnetic field. However, the i_{dref} provided by (4) varies only with speed, remaining constant at a fixed speed without adaptive adjustments as load changes. In other words, i_{dref} only considers the speed regulation requirement without accounting for load demands. A detailed analysis will be conducted with the help of Fig. 3.

As shown in Fig. 3, when the motor operates in the field weakening region at speed ω_{f}, (4) corresponds to the straight line $i_{\mathrm{d}} = i_{\mathrm{d\_f}}$ in the i_{d}–i_{q} plane, so the i_{d} used at speed ω_{f} remains constant at $i_{\mathrm{d\_f}}$. When the motor maintains the speed ω_{f}, the no-load operating point is f ($i_{\mathrm{d\_f}}$, 0), and the maximum load operating point is f* ($i_{\mathrm{d\_f}}$, $i_{\mathrm{q\_f}}$), indicating that as the load increases, the operating point reaches f* along line segment f–f*. The variation range of i_{q} is limited to [0, $i_{\mathrm{q\_f}}$]. However, the optimal no-load operating point at speed ω_{f} is j ($i_{\mathrm{d\_j}}$, 0) because point j can keep the same speed ω_{f} with the minimum i_{d} (j is the intersection between the regular hexagonal voltage constraint and the i_{d}-axis, $|i_{\mathrm{d\_j}}| < |i_{\mathrm{d\_f}}|$). The optimal maximum-load operating point is e* ($i_{\mathrm{d\_e}}$, $i_{\mathrm{q\_e}}$) because point e* can carry the maximum load $k_{\mathrm{t}}i_{\mathrm{q\_e}}$ at the same speed (e* is the intersection between the regular hexagonal voltage and current constraints, $i_{\mathrm{q\_e}} > i_{\mathrm{q\_f}}$).

The abovementioned analysis indicates that because the conventional formula-based field-weakening method only considers the speed regulation requirement without accounting for load demands, it leads to an undesirable allocation of d- and q-axis currents, resulting in poor current control trajectories. This reduces the flexibility in adjusting the motor's operating point, causing the actual operating point to deviate from the optimal position under different speeds and loads. On the one hand, this leads to a higher i_{d} during high-speed and low-load operations compared to the minimum i_{d} required to maintain the same speed. On the other hand, this results in a smaller actual load-carrying capability during field weakening operation than the ideal load-carrying capacity. The full potential of the motor's operational region is not thoroughly utilized, further reducing the motor's speed regulation range and load-carrying capacity under the existing method.

III. PROPOSED EXPANDED LIMIT BOUNDARY EMP-DSC METHOD

To address the existing method's problems and achieve a wider speed range and higher load capability, this article proposes an expanded limit boundary EMP-DSC method by improving linear constraints and the field-weakening approach. The following are the specific steps of the proposed method.

Step 1: Construct the predictive model. Considering parameter mismatches and external disturbances, the electrical and mechanical dynamics of the surface-mounted PMSM are

$$\begin{cases} \dot{i}_{\mathrm{d}} = L_0^{-1}\left(u_{\mathrm{d}} - R_0 i_{\mathrm{d}} + L_0 i_{\mathrm{q}}\omega_{\mathrm{e}} + \gamma_{\mathrm{d}}\right) \\ \dot{i}_{\mathrm{q}} = L_0^{-1}\left(u_{\mathrm{q}} - R_0 i_{\mathrm{q}} - L_0 i_{\mathrm{d}}\omega_{\mathrm{e}} - \psi_{\mathrm{f0}}\omega_{\mathrm{e}} + \gamma_{\mathrm{q}}\right) \\ \dot{\omega} = J_{\mathrm{r0}}^{-1}\left(k_{\mathrm{t0}} i_{\mathrm{q}} - T_{\mathrm{L}} + \gamma_{\omega}\right) \end{cases} \tag{5}$$

where R_0, L_0, ψ_{f0}, J_{r0}, and k_{t0} are nominal values of stator resistance, inductance, permanent magnet flux linkage, the moment of inertia, and torque constant, respectively; T_{L} is the load torque; electric angular speed $\omega_{\mathrm{e}} = p\omega$, and p is the number of pole pairs; γ_{d}, γ_{q}, and γ_{ω} are the lumped disturbances due to parameter variations and model mismatches.

To improve the controller's robustness and eliminate nonlinear coupling terms between speed and current for model linearization, model (5) can be transformed into first-order ultralocal equations using model-free control theory [23]

$$\begin{cases} \dot{i}_{\mathrm{d}} = \alpha_{\mathrm{i}} u_{\mathrm{d}} + F_{\mathrm{d}} \\ \dot{i}_{\mathrm{q}} = \alpha_{\mathrm{i}} u_{\mathrm{q}} + F_{\mathrm{q}} \\ \dot{\omega} = \alpha_{\omega} i_{\mathrm{q}} + F_{\omega} \end{cases} \tag{6}$$

where scaling factors $\alpha_{\mathrm{i}} = L_0^{-1}$, $\alpha_{\omega} = k_{\mathrm{t0}} J_{\mathrm{r0}}^{-1}$; $\boldsymbol{F} = [F_{\mathrm{d}} \quad F_{\mathrm{q}} \quad F_{\omega}]^{\mathrm{T}}$ represent the other known and unknown parts of the equations, and their estimated values $\hat{\boldsymbol{F}} = [\hat{F}_{\mathrm{d}} \quad \hat{F}_{\mathrm{q}} \quad \hat{F}_{\omega}\ ]^{\mathrm{T}}$ can be obtained through observers.

Equation (6) is a low parameter-dependent linear equation for PMSM, based on which the PMSM's ultralocal predictive model can be constructed as

$$\begin{cases}\boldsymbol{x}\left(k+1\right)=\boldsymbol{A}\boldsymbol{x}(k)+\boldsymbol{B}\boldsymbol{u}(k)\\ \boldsymbol{x}(k)=\Big[\ i_{\mathrm{d}}(k)\ i_{\mathrm{q}}(k)\ \omega(k)\ u_{\mathrm{d}}(k)\ u_{\mathrm{q}}(k)\\ \hat{F}_{\mathrm{d}}(k)\ \hat{F}_{\mathrm{q}}(k)\ \hat{F}_{\omega}(k)\ \omega_{\mathrm{ref}}(k)\ i_{\mathrm{dref}}(k)\Big]^{\mathrm{T}}\\ \boldsymbol{u}(k)=\left[\Delta u_{\mathrm{d}}(k)\ \Delta u_{\mathrm{q}}(k)\right]^{\mathrm{T}}\end{cases}$$

$$\begin{cases}\boldsymbol{A}=\begin{bmatrix}1 & 0 & 0 & T_{\mathrm{s}}\alpha_{\mathrm{i}} & 0 & & 0 & 0\\ 0 & 1 & 0 & 0 & T_{\mathrm{s}}\alpha_{\mathrm{i}} & T_{\mathrm{s}}\boldsymbol{I}_{3\times 3} & 0 & 0\\ 0 & T_{\mathrm{s}}\alpha_{\omega} & 1 & 0 & 0 & & 0 & 0\\ & & & \boldsymbol{0}_{7\times 3} & & & & \boldsymbol{I}_{7\times 7}\end{bmatrix}\\ \boldsymbol{B}=\left[\boldsymbol{0}_{2\times 3}\ \boldsymbol{I}_{2\times 2}\ \boldsymbol{0}_{2\times 5}\right]^{\mathrm{T}}\end{cases}\tag{7}$$

where $\boldsymbol{x}$ and $\boldsymbol{u}$ are the state and control vectors, respectively; T_{s} is the control period. To achieve speed tracking control with field-weakening operation, the speed reference ω_{ref} and d-axis current reference i_{dref} are used as the DSC system's dual reference inputs. The voltage increments $\Delta u_{\mathrm{d}}(k)=u_{\mathrm{d}}(k+1)-u_{\mathrm{d}}(k)$ and $\Delta u_{\mathrm{q}}(k)=u_{\mathrm{q}}(k+1)-u_{\mathrm{q}}(k)$ are control variables, and u_{d} and u_{q} are augmented into $\boldsymbol{x}$.

Step 2: Design the quadratic cost function J. The EMP algorithm obtains the optimal control sequences by minimizing J. Therefore, J should represent the comprehensive control objectives, including speed tracking, load balancing, and field-weakening current control

$$J=\sum_{i=0}^{N_{\mathrm{p}}}\boldsymbol{x}^{\mathrm{T}}\left(k+i\right)\boldsymbol{Q}\boldsymbol{x}\left(k+i\right)+\sum_{\mathrm{j}=0}^{N_{\mathrm{p}}-1}\boldsymbol{u}^{\mathrm{T}}\left(k+\mathrm{j}\right)\boldsymbol{R}\boldsymbol{u}\left(k+\mathrm{j}\right)$$

$$\begin{cases}\boldsymbol{Q}=\begin{bmatrix}q_{\mathrm{d}} & 0 & 0 & & 0 & 0 & -q_{\mathrm{d}}\\ 0 & \alpha_{\omega}q_{\mathrm{q}} & 0 & \boldsymbol{0}_{3\times 4} & -q_{\mathrm{q}} & 0 & 0\\ 0 & 0 & q_{\omega} & & 0 & -q_{\omega} & 0\\ & & & \boldsymbol{0}_{4\times 10} & & & \\ 0 & -q_{\mathrm{q}} & 0 & & \alpha_{\omega}^{-1}q_{\mathrm{q}} & 0 & 0\\ 0 & 0 & -q_{\omega} & \boldsymbol{0}_{3\times 4} & 0 & q_{\omega} & 0\\ -q_{\mathrm{d}} & 0 & 0 & & 0 & 0 & q_{\mathrm{d}}\end{bmatrix}\\ \boldsymbol{R}=\begin{bmatrix}q_{\mathrm{u}} & 0\\ 0 & q_{\mathrm{u}}\end{bmatrix}\end{cases}\tag{8}$$

where N_{p} is the predictive horizon; $\boldsymbol{Q}$ and $\boldsymbol{R}$ are the weighting matrices penalizing $\boldsymbol{x}$ and $\boldsymbol{u}$; q_{d}, q_{q}, q_{ω}, and q_{u} are weighting factors of i_{d}, i_{q}, ω, and $u_{\mathrm{d/q}}$, respectively. To understand more intuitively how the cost function works, the cost function in matrix form (8) can be transformed into weighted form.

Step 3: Improve the system's linear constraints. To overcome the limitations of conventional regular hexagonal constraints that restrict the motor's operational region and reduce the speed range and load capacity, the proposed method constructs irregular hexagonal current and voltage constraints, as shown in Fig. 4. Considering that the motor's motoring operation locates in the i_{d}–i_{q} plane's second quadrant, three current constraint segments (A–C, C–D, D–B) are used to approximate the current limit circle in the second quadrant to expand the operational region's limit boundary. In the remaining first, third, and fourth quadrants, only one segment is used to replace the current limit circle. Similarly, in the u_{d}–u_{q} plane's first quadrant, three voltage constraint segments (U–V, V–W, W–L) are used to approximate the voltage limit circle. In the remaining second, third, and fourth quadrants, only one segment is used to replace the voltage limit circle. The irregular hexagonal constraints are composed of one-quarter regular dodecagon and three-quarter square. Fig. 4 shows their specific shapes and positions in the u_{d}–u_{q} and i_{d}–i_{q} planes. The resulting linear equations for the irregular hexagonal current and voltage constraints are

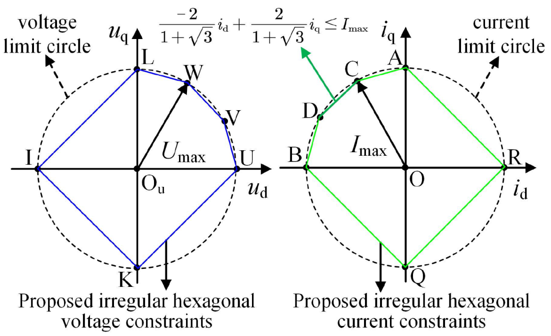

Fig. 4. Proposed irregular hexagon voltage and current constraints.

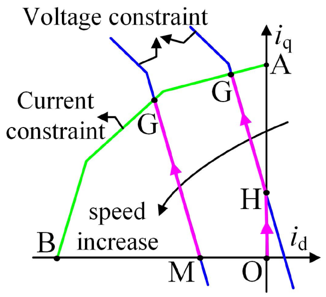

Fig. 5. Proposed optimal trajectories for field weakening.

$$\boldsymbol{A}_{\mathrm{v}}\begin{bmatrix}u_{\mathrm{d}}(k)\\ u_{\mathrm{q}}(k)\end{bmatrix}\leq\boldsymbol{E}\cdot U_{\mathrm{max}},\boldsymbol{A}_{\mathrm{i}}\begin{bmatrix}i_{\mathrm{d}}(k)\\ i_{\mathrm{q}}(k)\end{bmatrix}\leq\boldsymbol{E}\cdot I_{\mathrm{max}}\tag{9}$$

$$\begin{cases}\boldsymbol{A}_{\mathrm{v}}=\begin{bmatrix}-1 & -1 & 1 & 1 & \frac{2}{1+\sqrt{3}} & 2-\sqrt{3}\\ 1 & -1 & -1 & 2-\sqrt{3} & \frac{2}{1+\sqrt{3}} & 1\end{bmatrix}^{\mathrm{T}}\\ \boldsymbol{A}_{\mathrm{i}}=\begin{bmatrix}1 & 1 & -1 & -1 & \frac{-2}{1+\sqrt{3}} & \sqrt{3}-2\\ 1 & -1 & -1 & 2-\sqrt{3} & \frac{2}{1+\sqrt{3}} & 1\end{bmatrix}^{\mathrm{T}}.\end{cases}.$$

Step 4: Optimize the field-weakening method. Considering that the quality of current allocation directly affects the performance of field weakening operation [21], the proposed method utilizes the new voltage constraints to design a practical and simple optimal-trajectory field-weakening method that comprehensively considers speed regulation and load balancing, maintaining the motor's actual operating point near the optimal position. As shown in Fig. 5, the proposed optimal trajectories for field-weakening operation are defined as follows.

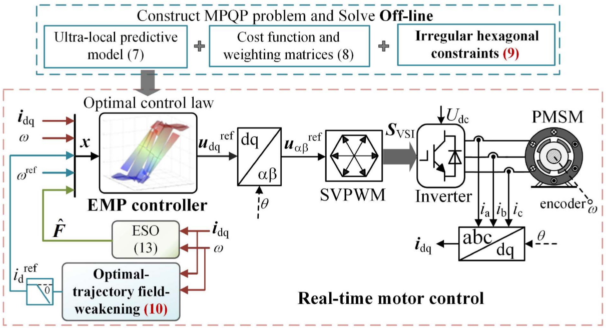

Fig. 6. Expanded limit boundary EMP-DSC controller construction process.

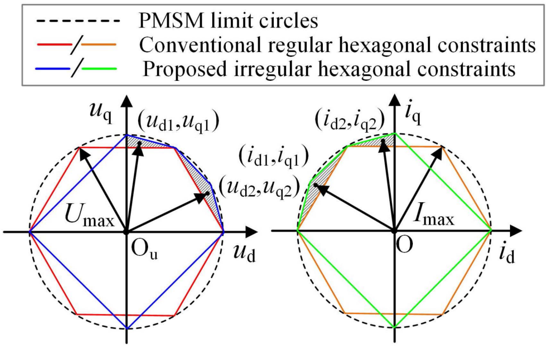

Fig. 7. Comparison of the proposed irregular hexagonal constraints and conventional regular hexagonal constraints.

1) In the low-speed stage of the field weakening region, the voltage constraint intersects the positive half-axis of the i_q-axis at point H. In this case, the optimal trajectory is set as line O–H–G, where point G is the intersection between the voltage and current irregular hexagonal constraints.
2) In the high-speed stage of the field weakening region, point H is lost, but the voltage constraint intersects the negative half-axis of the i_d-axis at point M. In this case, the optimal trajectory is set as line M–G.

The calculation formula of i_dref in the proposed optimal-trajectory field-weakening method is obtained directly by mathematically transforming the voltage constraint equation $u_\mathrm{d} + (2-\sqrt{3})u_\mathrm{d} = U_\mathrm{max}$ to

$$i_\mathrm{dref} = \frac{\left(\sqrt{3}-2\right) R_0 \psi_\mathrm{f0}\omega_e + U_\mathrm{max}\sqrt{R_0^2 + \left(\omega_e L_0\right)^2} - L_0\psi_\mathrm{f0}\omega_\mathrm{e}^2}{R_0^2 + \left(\omega_e L_0\right)^2} + \left(\sqrt{3}-2\right) i_\mathrm{q}. \tag{10}$$

If i_dref calculated by (10) is greater than zero, output $i_\mathrm{dref} = 0$, otherwise output the calculated value.

Step 5: Construct the expanded limit boundary EMP-DSC controller. The controller construction process is shown in Fig. 6. Based on the ultralocal predictive model (7), cost function (8), and the proposed irregular hexagonal constraints (9), the optimal speed-tracking problem for the EMP-DSC system can be obtained

$$\min_{\boldsymbol{U}=[\boldsymbol{u}^\mathrm{T}(0)\cdots\boldsymbol{u}^\mathrm{T}(N_\mathrm{p}-1)]^\mathrm{T}} J$$
$$\text{s.t.} \begin{cases} \boldsymbol{x}(k+i+1) = \boldsymbol{A}\boldsymbol{x}(k+i) + \boldsymbol{B}\boldsymbol{u}(k+i) \\ \boldsymbol{A}_\mathrm{v}\begin{bmatrix} u_\mathrm{d}(k) \\ u_\mathrm{q}(k)\end{bmatrix} \le U_\mathrm{max}\boldsymbol{E}, \boldsymbol{A}_\mathrm{i}\begin{bmatrix} i_\mathrm{d}(k) \\ i_\mathrm{q}(k)\end{bmatrix} \le I_\mathrm{max}\boldsymbol{E} \end{cases} \tag{11}$$

where $\boldsymbol{U}$ is the optimal control sequence.

By solving the MPQP problem (11) offline, CRs, and their corresponding optimal control laws $\boldsymbol{u}_\mathrm{opt}$ can be obtained as

$$\boldsymbol{u}_\mathrm{opt} = \boldsymbol{f}_a\boldsymbol{x}(k) + \boldsymbol{g}_a, \boldsymbol{x} \in \mathrm{CR}_a \tag{12}$$

where a is the index number of the CR; $\boldsymbol{f}_a$ and $\boldsymbol{g}_a$ are the optimal solution matrices; $\boldsymbol{f}_a = [k_\mathrm{d1}\cdots k_\mathrm{d10}; k_\mathrm{q1}\cdots k_\mathrm{q10}]_{2\times 10}$ consists of multiple feedback gain factors.

During online operation, the CR of the current state vector $\boldsymbol{x}$ is judged, and the optimal control law is obtained by looking up the table. The $\hat{\boldsymbol{F}}$ in $\boldsymbol{x}$ can be provided in real time by the auxiliary ESO, which is designed as

$$\begin{cases} \hat{\boldsymbol{x}}_\mathrm{o}(k+1) = \boldsymbol{A}_\mathrm{o}\hat{\boldsymbol{x}}_\mathrm{o}(k) + T_\mathrm{s}\hat{\boldsymbol{F}}(k) + \boldsymbol{B}_\mathrm{o}\boldsymbol{u}_\mathbf{o} + T_\mathrm{s}\boldsymbol{K}_1\boldsymbol{e}_\mathrm{x}(k) \\ \hat{\boldsymbol{F}}(k+1) = \hat{\boldsymbol{F}}(k) + T_\mathrm{s}\boldsymbol{K}_2\boldsymbol{e}_\mathrm{x}(k) \end{cases} \tag{13}$$

where $\boldsymbol{x}_\mathrm{o}(k) = [i_\mathrm{d}(k)\ i_\mathrm{q}(k)\ \omega(k)]^\mathrm{T}$; $\hat{\boldsymbol{x}}_\mathrm{o}$ is the estimated value of $\boldsymbol{x}_\mathrm{o}$; $\boldsymbol{e}_\mathrm{x} = \boldsymbol{x}_\mathrm{o} - \hat{\boldsymbol{x}}_\mathrm{o}$ is the observation error; $\boldsymbol{u}_\mathbf{o}(k) = [u_\mathrm{d}(k)\ u_\mathrm{q}(k)]^\mathrm{T}$; Matrices $\boldsymbol{A}_\mathrm{o}$ and $\boldsymbol{B}_\mathrm{o}$ are

$$\boldsymbol{A}_\mathrm{o} = \begin{bmatrix} 1 & 0 & 0 \\ 0 & 1 & 0 \\ 0 & T_\mathrm{s}\alpha_\omega & 1 \end{bmatrix}, \boldsymbol{B}_\mathrm{o} = \begin{bmatrix} T_\mathrm{s}\alpha_\mathrm{i} & 0 \\ 0 & T_\mathrm{s}\alpha_\mathrm{i} \\ 0 & 0 \end{bmatrix}. \tag{14}$$

$\boldsymbol{K}_1 = \mathrm{diag}[h_{11}, h_{11}, h_{13}]$ and $\boldsymbol{K}_2 = \mathrm{diag}[h_{21}, h_{21}, h_{23}]$ are the ESO's gain matrices. The observed values' convergence can be guaranteed by selecting these gains properly [24].

IV. PERFORMANCE ANALYSIS OF THE PROPOSED EMP-DSC METHOD

A. *Irregular Hexagonal Constraints Expand Limit Boundary*

The proposed irregular hexagonal voltage and current constraints are shown in Fig. 7. It can be observed from Fig. 7 that the voltage vectors terminating at points (u_d1, u_q1) and (u_d2, u_q2), as well as the current vectors terminating at points (i_d1, i_q1) and (i_d2, i_q2), are not reachable under the conventional regular hexagonal constraints but can still be utilized under the proposed constraints. Compared to the conventional constraints, the proposed irregular hexagonal constraints expand the voltage vectors' reachable region in the u_d–u_q plane's first quadrant and the current vectors' reachable region in the i_d–i_q plane's second quadrant both by 15.47%.

Fig. 8 illustrates the changes in the operational region and limit boundaries as speed increases. Next, three typical operating conditions are provided to demonstrate the system performance's comprehensive enhancement due to the proposed

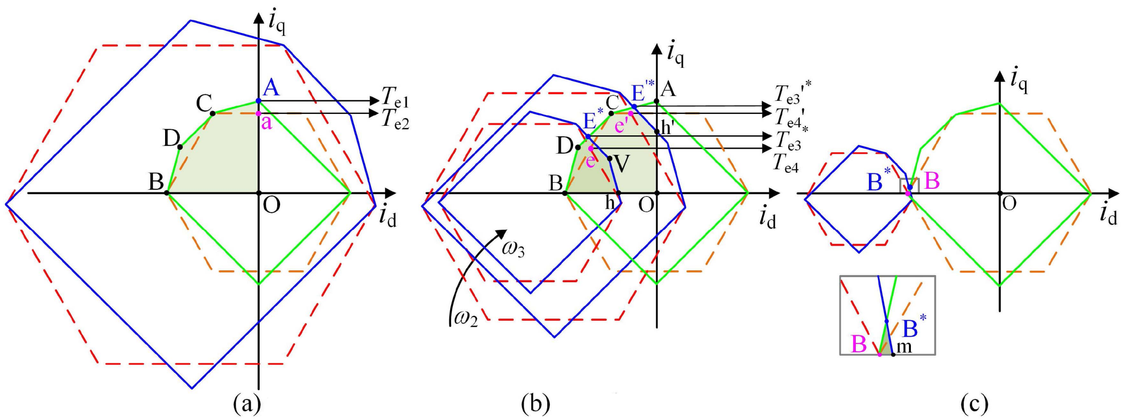

Fig. 8. PMSM's operational region and limit boundaries under the proposed irregular hexagonal constraints. (a) ω_1. (b) ω_2 and ω_3. (c) ω_4.

irregular hexagonal constraints. The four speeds in Fig. 8 are identical to those in Fig. 2.

1) As shown in Fig. 8(a), when the motor operates in the constant torque region (e.g., $\omega = \omega_1$), its operational region is the polygon O–A–C–D–B under irregular hexagonal constraints, significantly expanding the motor's operational region compared to the conventional constraints. Due to the $i_d = 0$ control strategy, the actual operational region is line segment O–A. Consequently, the motor's operating point is no longer limited to point a but can reach point A, allowing the motor to obtain the maximum q-axis current $I_{\max}$. Correspondingly, the maximum available torque in the constant torque region is restored to the limit value T_{e1}. Hence, under the proposed method, the motor's load-carrying capacity in the constant torque region is 1.15 times that of the existing method, representing a 15.47% increase.

2) As shown in Fig. 8(b), when the motor operates in the field weakening region (e.g., $\omega = \omega_2$ and $\omega = \omega_3$), its operational regions are polygons O–h'–E'^{*}–C–D–B and h–V–E^{*}–D–B under irregular hexagonal constraints, respectively, significantly expanding the motor's operational region compared to the conventional constraints. The intersection points between the proposed voltage and current constraints are E'^{*} and E^{*}, while the intersection points between conventional voltage and current constraints remain as e' and e. Thus, compared to conventional constraints, the proposed constraints improve the ideal maximum load-carrying capability from T_{e4}' (T_{e4}) corresponding to point e' (e) to $T_{e3}{}'^{*}$ ($T_{e3}{}^{*}$) corresponding to point E'^{*} (E^{*}) when maintaining speed ω_2 (ω_3). Similarly, it can be deduced that, compared to conventional constraints, the proposed irregular hexagonal constraints enhance the ideal maximum load capacity at all speeds during the field weakening operation.

3) As shown in Fig. 8(c), when the motor reaches its maximum speed ω_4 under the conventional regular hexagonal constraints, the intersection between the proposed irregular hexagonal voltage and current constraints is point B^{*}, which still lies in the second quadrant. Thus, a feasible operational region, the polygon m–B^{*}–B, allows the motor to continue accelerating until point B^{*} coincides with point B. Consequently, the proposed irregular hexagonal constraints enhance the motor's ideal maximum achievable speed, expanding the speed regulation range compared to conventional constraints.

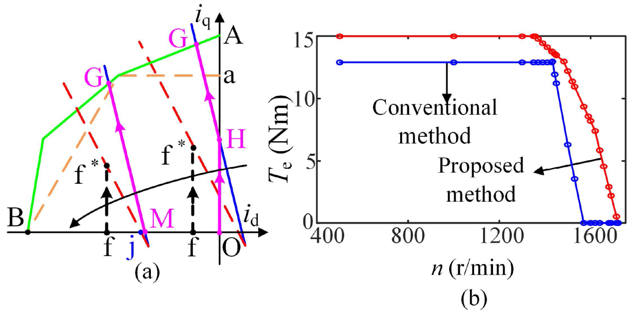

Fig. 9. (a) Control trajectories under conventional and proposed methods. (b) Torque-speed curves of existing and proposed methods.

B. Optimal-Trajectory Field-Weakening Method Optimizes Current Allocation

The motor's actual operating point depends heavily on the field weakening implementation method. The control trajectories of the conventional formula-based field-weakening method and the proposed optimal-trajectory field-weakening method are compared in Fig. 9(a). The control trajectories under the proposed method are O–H–G and M–G. In contrast, the control trajectory under the existing method is f–f^{*}.

As shown in Fig. 9(a), the proposed method skillfully uses the linear voltage constraint, whose equation is known, as the optimal trajectory for field weakening operation. According to these optimal trajectories, on the one hand, the minimum i_d required to maintain the corresponding speed is utilized during light-load operation in the field weakening low-speed stage (corresponding to segment O–H) and no-load operation in the field weakening high-speed stage (corresponding to point M). Therefore, the i_d used by the proposed method is smaller than

TABLE I
PARAMETERS OF THE SURFACE-MOUNTED PMSM

Parameter	Value	Parameter	Value
Rated power P_{N}	3.1 Kw	Rated speed ω_{N}	1370r/min
Rated current I_{N}	13.5 A	Pole pairs	2
Rated torque T_{eN}	15 N·m	Stator inductance L_0	4.4 mH
Torque constant k_{t0}	1.11 N·m/A	Stator resistance R_0	0.48 Ω
Total inertia J_{r0}	0.028 kg·m^2	Flux linkage ψ_{f0}	0.369 Wb

that of the existing method because the abscissa of point O or M is smaller than point f. On the other hand, as the load increases, the i_{d} will adaptively increase to obtain a larger i_{q} until reaching the maximum load point G at the corresponding speed, which means that the degree of freedom in adjusting the motor's operating point is increased, the current allocation is optimized, and the dual requirements of speed tracking and load balancing can be comprehensively considered on the premise of satisfying the dual constraints of current and voltage, maintaining the actual operating point near the optimal operating point and making full use of the motor's operational range. Therefore, the load capability under the proposed method is improved.

With the help of MATLAB, the motor's torque-speed curves under existing and proposed methods are plotted in Fig. 9(b), with the motor parameters listed in Table I. Fig. 9(b) visually illustrates that the proposed method widens the motor's limit boundary, expands the speed regulation range, and increases the load capacity simultaneously, compared to the existing method.

Moreover, the irregular hexagonal constraints and the optimal-trajectory field-weakening method complement each other. The new constraints expand the limit boundary and provide the linear optimal trajectories. The new field weakening method fully leverages the enlarged operational region, ensuring that the actual operating point covers the entire operational region and lies near the optimal point. Furthermore, the proposed irregular hexagonal constraints do not increase the system's constraint dimension, thereby avoiding an increase in algorithmic complexity. The proposed optimal trajectories are defined by known linear equations. So, there is no need to solve the intersection between current and voltage constraints and intersections between the constraints and the coordinate axis in real time. The field weakening implementation is simple and does not increase the algorithm's complexity. The proposed method enhances the capabilities and performance of the extreme operations under EMP-DSC, thus reinforcing its practicality and competitiveness in servo drives.

C. Stability Proof of the Entire Control System

The entire control block diagram of the proposed EMP-DSC method is shown in Fig. 10. As shown in Fig. 10, the overall control system consists of the following three parts: the EMP control law, the ESO, and the controlled plant. The optimal control law used by the EMP controller is an explicit piecewise affine function of the states and can be accurately obtained. Therefore, according to the principle of control theory, a discrete-time system is stable if all its closed-loop poles locate within the unit circle of the z-plane [25]. Therefore, the entire control system's stability can be proved and guaranteed with the help of the closed-loop transfer function.

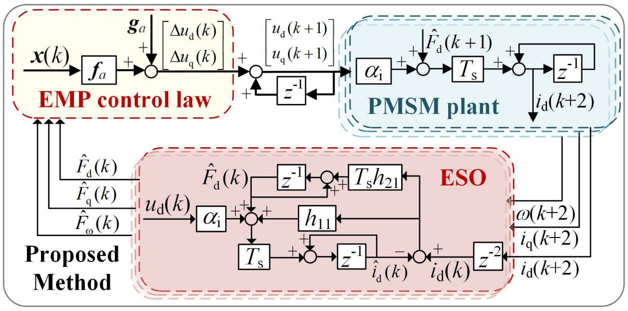

Fig. 10. Entire control block diagram of the proposed method with the ESO and EMP-DSC controller.

By applying the z-transform and mathematical organization on the controlled plant (6), ESO (13), and the EMP control law (12), the closed-loop characteristic equations of the entire control system's d and q-axes can be obtained as

$$\begin{cases} P_{\mathrm{closed}} = P_{\mathrm{ESOd}} P_{\mathrm{cond}} \\ P_{\mathrm{ESOd}} = z^2 + \left(T_{\mathrm{s}} h_{11} - 2\right) z + T_{\mathrm{s}}^2 h_{21} - T_{\mathrm{s}} h_{11} + 1 \\ P_{\mathrm{cond}} = z^2 - \left(k_{\mathrm{d}4} + 2\right) z + k_{\mathrm{d}4} + 1 - T_{\mathrm{s}} \alpha_{\mathrm{i}} k_{\mathrm{d}1} \end{cases} \tag{15}$$

and

$$\begin{cases} P_{\mathrm{closeq}} = P_{\mathrm{ESOq}} P_{\mathrm{conq}} \\ P_{\mathrm{ESOq}} = z^2 + \left(T_{\mathrm{s}} h_{13} - 2\right) z + T_{\mathrm{s}}^2 h_{23} - T_{\mathrm{s}} h_{13} + 1 \\ P_{\mathrm{conq}} = z^3 - \left(k_{\mathrm{q}5} + 3\right) z^2 + \left(2k_{\mathrm{q}5} + 3 - k_{\mathrm{q}2} T_{\mathrm{s}} \alpha_{\mathrm{i}}\right) z \\ \qquad + \left(k_{\mathrm{q}2} T_{\mathrm{s}} \alpha_{\mathrm{i}} - T_{\mathrm{s}}^2 \alpha_{\omega} \alpha_{\mathrm{i}} k_{\mathrm{q}3} - k_{\mathrm{q}5} - 1\right) \end{cases} \tag{16}$$

where P_{closed} is the d-axis closed-loop characteristic equation, and P_{closeq} is the q-axis closed-loop characteristic equation.

Equations (15) and (16) show that both characteristic equations consist of two parts: one part is the ESO's characteristic equation P_{ESOd} (P_{ESOq}) exactly, and the other part is P_{cond} (P_{conq}) related to the feedback gain factors of the EMP controller. According to the control theory principles, if the roots of all parts lie inside the z-plane's unit circle, the whole system is stable. The entire system's stability conditions are easily obtained according to the Jury criterion [26], [27]

$$\begin{cases} h_{11} < 2T_{\mathrm{s}}^{-1}, h_{13} < 2T_{\mathrm{s}}^{-1} \\ 0 < h_{21} < T_{\mathrm{s}}^{-1} h_{11}, 0 < h_{23} < T_{\mathrm{s}}^{-1} h_{13}, k_{\mathrm{d}1} < 0, k_{\mathrm{q}3} < 0 \\ \frac{T_{\mathrm{s}} \alpha_{\mathrm{i}} k_{\mathrm{d}1}}{2} - 2 < k_{\mathrm{d}4} < T_{\mathrm{s}} \alpha_{\mathrm{i}} k_{\mathrm{d}1}, P_{\mathrm{conq}}\left(-1\right) < 0 \\ \left|a_1\right| < 1, \left|a_1^2 - 1\right| > \left|a_1 a_2 - a_3\right| \end{cases} \tag{17}$$

where $a_1 = k_{\mathrm{q}2} T_{\mathrm{s}} \alpha_{\mathrm{i}} - T_{\mathrm{s}}^2 \alpha_{\omega} \alpha_{\mathrm{i}} k_{\mathrm{q}3} - k_{\mathrm{q}5} - 1$, $a_2 = -k_{\mathrm{q}5} - 3$, $a_3 = 2k_{\mathrm{q}5} + 3 - k_{\mathrm{q}2} T_{\mathrm{s}} \alpha_{\mathrm{i}}$.

Equation (17) is the stability conditions for the proposed control system. The entire control system is stable if the ESO gains and the EMP control law's feedback gain factors satisfy the stability conditions.

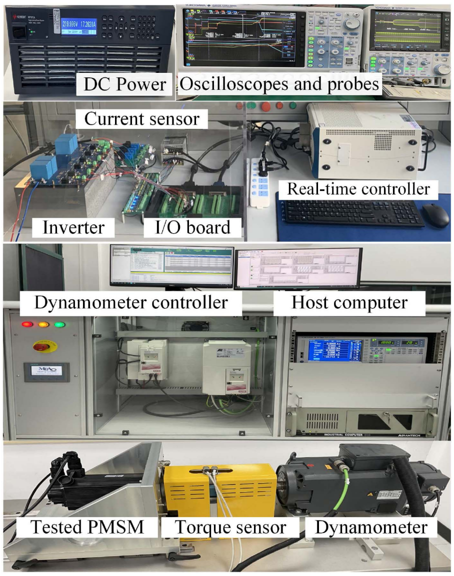

Fig. 11. Experiment platform.

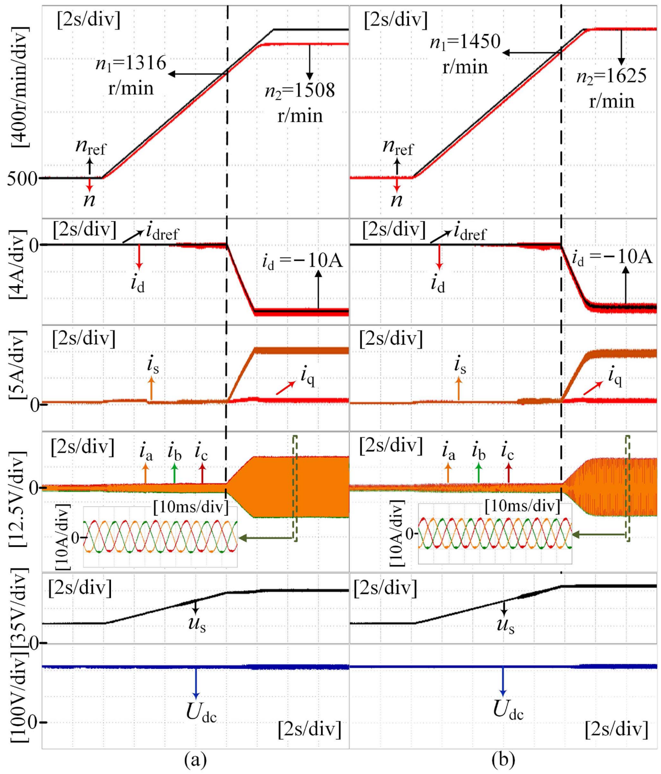

Fig. 12. Comparative experimental results of the no-load acceleration process. (a) Existing method. (b) Proposed method.

V. Experimental Results

To validate the proposed method's feasibility, hardware experiments are conducted on a PMSM test platform, as shown in Fig. 11. The surface-mounted PMSM's parameters are listed in Table I. The proposed EMP-DSC controller's parameters are

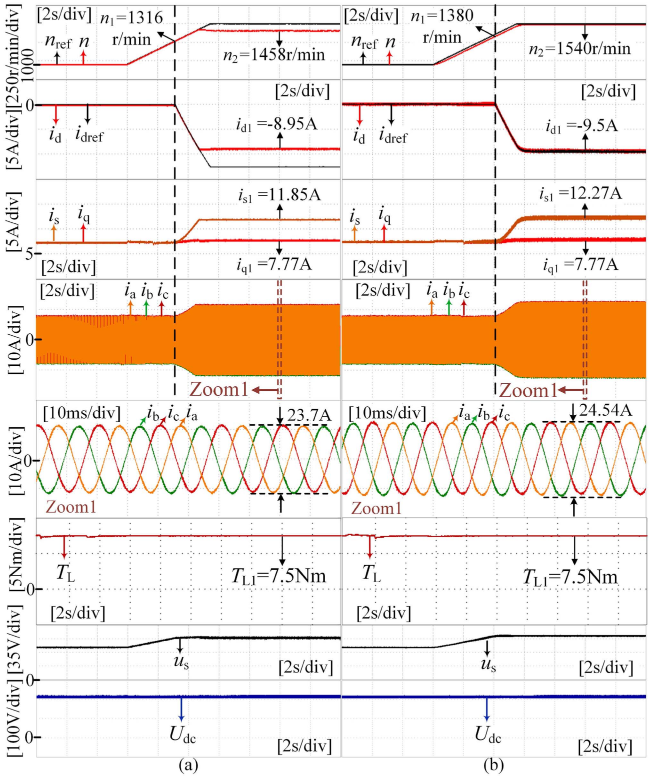

Fig. 13. Comparative experimental results of the constant-load acceleration process. (a) Existing method. (b) Proposed method.

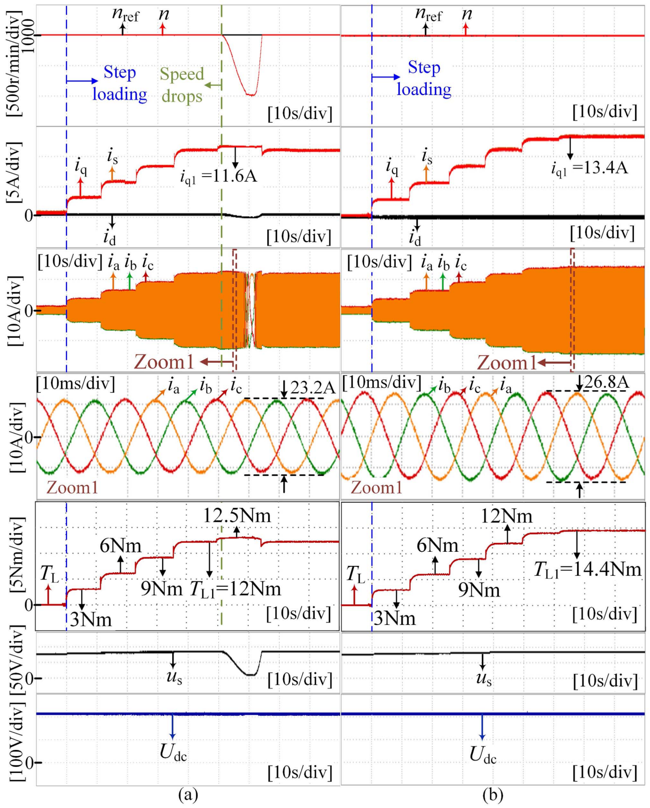

Fig. 14. Comparative experimental results of the constant-speed loading process in the constant-torque region. (a) Existing method. (b) Proposed method.

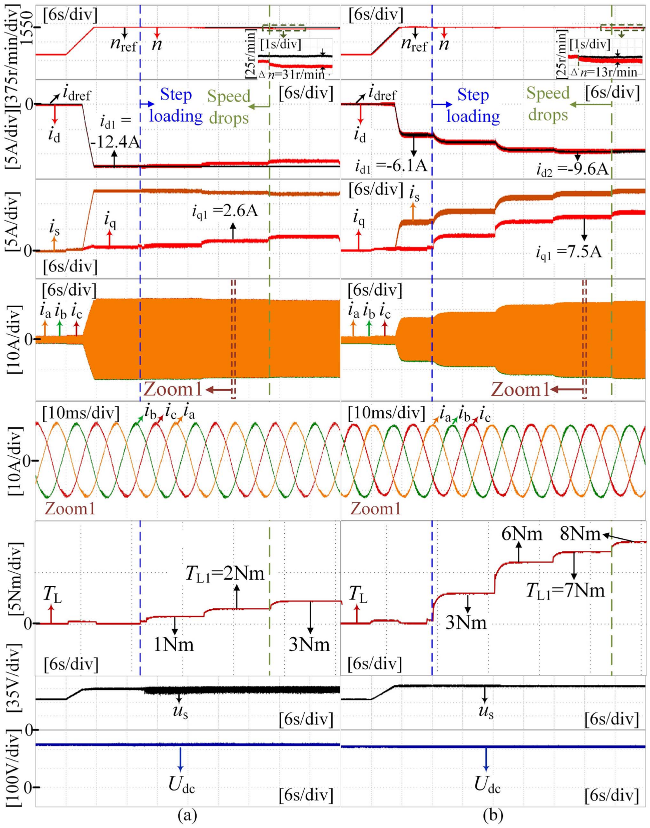

(a) (b)

Fig. 15. Comparative experimental results of the constant-speed loading process in the field-weakening region. (a) Existing method. (b) Proposed method.

set as $q_q = 10$, $q_d = 700$, $q_\omega = 20000$, and $q_u = 0.01$. $U_{dc} = 220$ V, $T_s = 100$ μs, $N_p = 5$. In order to strictly adhere to the principle of controlling variables in comparative experiments and to independently verify the beneficial effects of the proposed constraints and field-weakening method, the conventional predictive model used in [20] is replaced by the new hyperlocal predictive model defined by (7) and the resulting EMP-DSC method is treated as the existing method. Both the existing and proposed methods only consider linear modulation and use the same maximum allowable current and voltage, $I_{max} = I_N$, and $U_{max} = U_{dc}/\sqrt{3}$.

A. Speed Range Comparison

The no-load acceleration experiment and constant-load acceleration experiment are conducted separately to compare the speed regulation range of the existing and proposed methods, and comparative experimental results are shown in Figs. 12 and 13, respectively.

Fig. 12 shows the experimental results of the motor's no-load acceleration process. The speed command n_{ref} increases at a rate of 100 r/min/s from 500 r/min. From Fig. 12(a), it can be observed that the existing method starts using negative i_d when the speed reaches $n_1 = 1316$ r/min, and when i_{dref} is limited to -10 A, the maximum achievable speed is $n_2 = 1508$ r/min. Fig. 12(b) shows that the proposed method starts using negative i_d when the speed reaches $n_1 = 1450$ r/min, and when i_{dref} is limited to -10 A, the maximum achievable speed is $n_2 = 1625$ r/min. Compared to the existing method, the proposed method shifts the no-load field-weakening starting point by 155 r/min and expands the speed range by 117 r/min (a 7.7% increase) under the same d-axis field-weakening current. Results show that the proposed method delays the use of negative i_d and reduces the magnitude of i_d required to maintain the same speed, extending the motor's no-load speed regulation range.

Fig. 13 shows the experimental results of the motor's constant-load acceleration process. The load is maintained at 7.5 N·m (50% of the rated torque), and the speed command n_{ref} increases at a rate of 100 r/min/s from 1000 r/min. It can be seen from Fig. 13(a) that under the half-load condition, the existing method starts using negative i_d when the speed reaches $n_1 = 1316$ r/min, and the maximum achievable speed is $n_2 = 1458$ r/min, corresponding to $i_{s1} = 11.85$ A. Fig. 13(b) shows that under the half-load condition, the proposed method starts using negative i_d when the speed reaches $n_1 = 1380$ r/min, and the maximum achievable speed is $n_2 = 1540$ r/min, corresponding to $i_{s1} = 12.27$ A. Compared to the existing method, the proposed method shifts the half-load field weakening starting point by 64 r/min, increases the usable current vector magnitude by 0.42 A, and expands the speed range by 82 r/min (a 5.6% increase) under the same load condition. Results show that the proposed method also delays the use of negative i_d under load, and the speed range is improved due to the larger available $|i_s|$ under the expanded limit boundary.

B. Load Capacity Comparison

The constant-speed loading experiments are conducted, respectively, in constant-torque and field-weakening regions to compare the load capacity of the existing and proposed methods, and comparative experimental results are shown in Figs. 14 and 15, respectively.

Fig. 14 presents the experimental results of the motor's constant-speed loading process in the constant torque region. The speed is maintained at 1000 r/min, which is lower than the rated speed, and the load is step increased until reaching the maximum load. As shown in Fig. 14(a), when a load of $T_{L1} = 12$ N·m is applied, the motor can achieve a balance between electromagnetic torque and load torque. However, when the load increases to 12.5 N·m, although the existing method provides its maximum achievable q-axis current i_{q1} in the constant torque region, which is 11.6 A, the motor is unable to balance the load torque, resulting in a rapid drop in speed. Fig. 14(b) shows that the maximum achievable q-axis current with the proposed method is $i_{q1} = 13.4$ A in the constant torque region, and the corresponding maximum load capacity is $T_{e1} = 14.4$ N·m. Compared to the existing method, the proposed method increases the maximum achievable q-axis current and load capacity by 1.8 A and 2.4 N·m (a 20% increase), respectively. Results show that the proposed method enhances the motor's load capacity in the constant torque region by improving current constraints.

Fig. 15 presents the experimental results of the motor's constant-speed loading process in the field weakening region. The speed is maintained at 1550 r/min, which is higher than

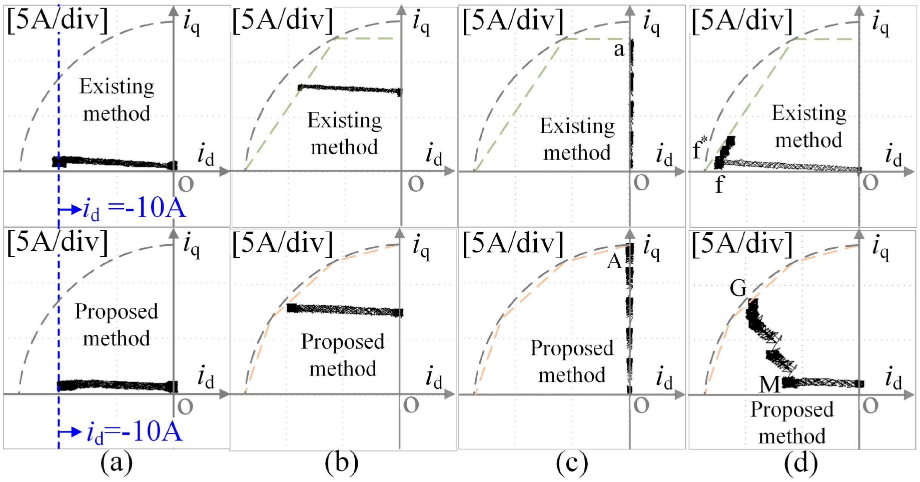

Fig. 16. Current control trajectories in the i_d–i_q plane. (a) No-load acceleration process. (b) Constant-load acceleration process. (c) Constant-speed loading process in the constant-torque region. (d) Constant-speed loading process in the field-weakening region.

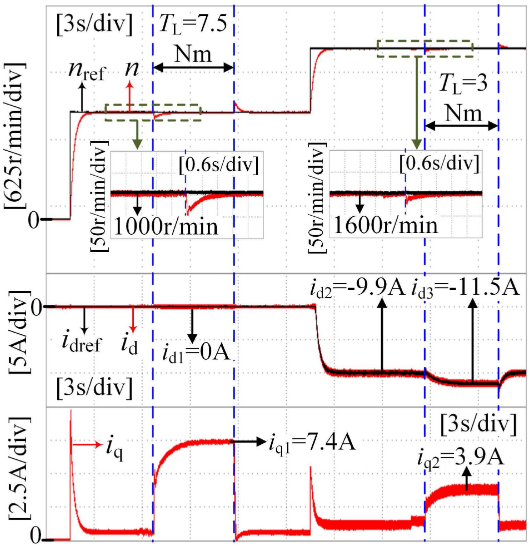

Fig. 17. Experimental results of step commands when parameters mismatch.

the rated speed, and the load is step increased. Fig. 15 indicates that when the motor operates at 1550 r/min without load, the field-weakening current required under the existing method is $i_{\mathrm{dref1}} = -12.4$ A, while the field-weakening current required under the proposed method is $i_{\mathrm{dref1}} = -6.1$ A, which demonstrates that the proposed method can keep the same speed with a smaller negative i_d. Fig. 15(a) shows that when maintaining the speed of 1550 r/min, the existing method can load up to $T_{L1} = 2$ N·m, corresponding to $i_{q1} = 2.6$ A. It is worth noting that when the load increases to 3 N·m, the motor can still balance the electromagnetic and load torques. However, this is accomplished by sacrificing the amplitude of i_d to increase the amplitude of i_q under the limitation of $|\boldsymbol{i}_s| \leq I_{\max}$. The reduction of $|i_d|$ results in the inability to maintain 1550 r/min and a speed drop. Fig. 15(b) shows that when maintaining the speed of 1550 r/min, the proposed method can load up to $T_{L1} = 7$ N·m, corresponding to $i_{q1} = 7.5$ A. Further increasing the load to 8 N·m also leads to a speed drop. Compared to the existing method, the proposed method increases the maximum load capacity and q-axis current by 3.87 N·m and 4.9 A (a 250% increase) at 1550 r/min. Results demonstrate that the proposed method significantly improves the motor's load capacity in the field weakening region.

C. *Current Control Trajectories Comparison*

The current control trajectories in the i_d–i_q plane of these four experimental processes are presented in Fig. 16. Fig. 16(a) shows current trajectories during the no-load acceleration process, where the negative i_d gradually increases to -10 A, while a small value of i_q is used for acceleration. Fig. 16(b) shows current trajectories during the constant-load acceleration process, where i_q is basically maintained constant to balance the fixed load and achieve acceleration. At the same time, negative i_d gradually increases to increase the speed until the trajectory reaches the limit boundary. Compared to the existing method, the proposed method can use a higher i_d and obtain a larger speed regulation range due to the expanded operational region. Fig. 16(c) shows current trajectories during the constant-speed loading process in the constant-torque region, where i_d is zero, while i_q gradually increases to balance the growing load. The existing method's trajectory terminates at point a, while the proposed method's trajectory terminates at point A. Fig. 16(d) depicts current trajectories during the constant-speed loading process in the field-weakening region. In Fig. 16(d), trajectories indicate that the i_d used in the existing method depends only on the speed and remains unchanged with load variations, resulting in a line segment f–f* perpendicular to the i_d-axis. (When the trajectory reaches the limit boundary, the increasing load will lead to a speed drop, causing the control trajectory to move along the voltage constraint.) While, the proposed method uses the minimum i_d required to maintain the corresponding speed, and the motor operates in the negative half-axis of the i_d-axis during no-load field-weakening operation. As the load increases, negative i_d and positive i_q simultaneously increase along the optimal trajectory M–G. Trajectories show that the proposed optimal-trajectory field weakening method allows for meeting dual requirements of speed regulation and load balancing while satisfying voltage and current constraints, optimizing the distribution of d- and q-axis currents, and improving field weakening performance.

D. Parameter Robustness Performance

Speed and load step experiments are conducted to verify the proposed method's parameter robustness. Experimental results in Fig. 17 illustrate that the proposed method can achieve offset-free speed tracking control with or without a load in both constant-torque and field-weakening regions, even in the case of parameter mismatches ($L = 0.65L_0$, $J_\mathrm{r} = 1.5J_{\mathrm{r}0}$). Results show that the proposed method exhibits excellent steady-state control accuracy, parameter robustness, and disturbance rejection capability.

VI. CONCLUSION

This article proposes the extended limit boundary EMP-DSC method to achieve the PMSM's excellent control of wide speed range and high-load capacity. The proposed method widens the operational region's limit boundary by constructing irregular hexagonal current and voltage constraints, thereby expanding speed and load ranges. Then, with the help of new constraints, the optimal-trajectory field-weakening method is introduced to take into account both speed adjustment and load balancing, which improves the current allocation. Experimental results demonstrate that the proposed method not only improves the field-weakening starting speeds, delaying the use of negative i_d and reducing the i_d required to maintain the same speed but also expands the motor's speed range under different loads. Moreover, the proposed method enhances the load capacity over the entire speed range, including the constant torque and field-weakening regions, optimizing current control trajectories and operational performance. This article thoroughly discusses the limitations of the existing EMP-DSC method and proposes targeted improvements to enhance the practicality and competitiveness of the EMP-DSC method in motor servo drive fields.

REFERENCES

[1] S. Lin, Y. Cao, Z. Wang, Y. Yan, T. Shi, and C. Xia, "Speed controller design for electric drives based on decoupling two-degree-of-freedom control structure," *IEEE Trans. Power Electron.*, vol. 38, no. 12, pp. 15996–16009, Dec. 2023.

[2] Z. Chen, Y. Yan, T. Shi, X. Gu, Z. Wang, and C. Xia, "An accurate virtual signal injection control for IPMSM with improved torque output and widen speed region," *IEEE Trans. Power Electron.*, vol. 36, no. 2, pp. 1941–1953, Feb. 2021.

[3] S. Chai, L. Wang, and E. Rogers, "A cascade MPC control structure for a PMSM with speed ripple minimization," *IEEE Trans. Ind. Electron.*, vol. 60, no. 8, pp. 2978–2987, Aug. 2013.

[4] B. Wang, M. Tian, Y. Yu, Q. Dong, and D. Xu, "Enhanced ADRC with quasi-resonant control for PMSM speed regulation considering aperiodic and periodic disturbances," *IEEE Trans. Transp. Electrific.*, vol. 8, no. 3, pp. 3568–3577, Sep. 2022.

[5] M. Zhao, Y. Cao, Y. Yan, Z. Zhang, T. Shi, and C. Xia, "Weighting factors tuning method in explicit model predictive direct speed control of permanent magnet synchronous motor," in *Proc. 24th Int. Conf. Elect. Mach. Syst.*, 2021, pp. 653–658.

[6] T. Guo, Z. Sun, X. Wang, S. Li, and K. Zhang, "A simple current-constrained controller for permanent-magnet synchronous motor," *IEEE Trans. Ind. Inform.*, vol. 15, no. 3, pp. 1486–1495, Mar. 2019.

[7] M. Zhao, S. Lin, Y. Cao, Z. Zhou, T. Shi, and C. Xia, "Explicit model predictive cascade-free direct force and torque control of quadrotors," *IEEE Trans. Ind. Electron.*, vol. 71, no. 4, pp. 3441–3451, Apr. 2024.

[8] M. Preindl and S. Bolognani, "Model predictive direct speed control with finite control set of PMSM drive systems," *IEEE Trans. Power Electron.*, vol. 28, no. 2, pp. 1007–1015, Feb. 2013.

[9] H. Kawai, Z. Zhang, R. Kennel, and S. Doki, "Direct speed control based on finite control set model predictive control with voltage smoother," *IEEE Trans. Ind. Electron.*, vol. 70, no. 3, pp. 2363–2372, Mar. 2023.

[10] L. Harnefors, S. E. Saarakkala, and M. Hinkkanen, "Speed control of electrical drives using classical control methods," *IEEE Trans. Ind. Appl.*, vol. 49, no. 2, pp. 889–898, Mar. 2013.

[11] L. Yang, H. Li, J. Huang, Z. Zhang, and H. Zhao, "Model predictive direct speed control with novel cost function for SMPMSM drives," *IEEE Trans. Power Electron.*, vol. 37, no. 8, pp. 9586–9595, Aug. 2022.

[12] H. Wang, J. Su, and G. Yang, "Line-constrained based explicit model predictive current control for IPMSMs drives," *IEEE Trans. Power Electron.*, vol. 38, no. 8, pp. 10093–10103, Aug. 2023.

[13] A. Bemporad, M. Morari, V. Dua, and E. Pistikopoulos, "The explicit linear quadratic regulator for constrained systems," *Automatica*, vol. 38, no. 1, pp. 3–20, Jan. 2002.

[14] P. Tøndel, T. A. Johansen, and A. Bemporad, "An algorithm for multi-parametric quadratic programming and explicit MPC solutions," *Automatica*, vol. 39, no. 3, pp. 489–497, Mar. 2003.

[15] P. Tøndel, T. Johansen, and A. Bemporad, "Evaluation of piecewise affine control via binary search tree," *Automatica*, vol. 39, pp. 945–950, May 2003.

[16] S. Bolognani, S. Bolognani, L. Peretti, and M. Zigliotto, "Design and implementation of model predictive control for electrical motor drives," *IEEE Trans. Ind. Electron.*, vol. 56, no. 6, pp. 1925–1936, Jun. 2009.

[17] M. Wang, J. Su, and K. Zhao, "Explicit model predictive control of permanent magnet synchronous motor with Kalman filter," in *Proc. 22nd Int. Conf. Elect. Mach. Syst.*, 2019, pp. 1–6.

[18] S. Lin, M. Zhao, Y. Cao, Z. Lin, T. Shi, and C. Xia, "Active disturbance rejection explicit model predictive direct speed control for permanent magnet synchronous motors," in *Proc. 25th Int. Conf. Elect. Mach. Syst.*, 2022, pp. 1–6.

[19] Z. Mynar, L. Vesely, and P. Vaclavek, "PMSM model predictive control with field-weakening implementation," *IEEE Trans. Ind. Electron.*, vol. 63, no. 8, pp. 5156–5166, Aug. 2016.

[20] J. Liu, C. Gong, Z. Han, and H. Yu, "IPMSM model predictive control in flux-weakening operation using an improved algorithm," *IEEE Trans. Ind. Electron.*, vol. 65, no. 12, pp. 9378–9387, Dec. 2018.

[21] M. Tursini, E. Chiricozzi, and R. Petrella, "Feedforward flux-weakening control of surface-mounted permanent-magnet synchronous motors accounting for resistive voltage drop," *IEEE Trans. Ind. Electron.*, vol. 57, no. 1, pp. 440–448, Jan. 2010.

[22] R. Nalepa and T. Orlowska-Kowalska, "Optimum trajectory control of the current vector of a nonsalient-pole PMSM in the field-weakening region," *IEEE Trans. Ind. Electron.*, vol. 59, no. 7, pp. 2867–2876, Jul. 2012.

[23] Y. Zhang, J. Jin, and L. Huang, "Model-free predictive current control of PMSM drives based on extended state observer using ultralocal model," *IEEE Trans. Ind. Electron.*, vol. 68, no. 2, pp. 993–1003, Feb. 2021.

[24] L. Qu, W. Qiao, and L. Qu, "An enhanced linear active disturbance rejection rotor position sensorless control for permanent magnet synchronous motors," *IEEE Trans. Power Electron.*, vol. 35, no. 6, pp. 6175–6184, Jun. 2020.

[25] K. Ogata, *Discrete-Time Control Systems*. Englewood Cliffs, NJ, USA: Prentice-Hall, 1995.

[26] S. Lin, Y. Cao, C. Li, Z. Wang, T. Shi, and C. Xia, "Two-degree-of-Freedom active disturbance rejection current control for permanent magnet synchronous motors," *IEEE Trans. Power Electron.*, vol. 38, no. 3, pp. 3640–3652, Mar. 2023.

[27] M. Tian, B. Wang, Y. Yu, Q. Dong, and D. Xu, "Discrete-time repetitive control-based ADRC for current loop disturbances suppression of PMSM drives," *IEEE Trans. Ind. Inform.*, vol. 18, no. 5, pp. 3138–3149, May 2022.

Mengyuan Zhao was born in Hebei, China, in 1997. She received the B.S. degree in electrical engineering from the Hebei University of Technology, Tianjin, China, in 2019. She is currently working toward the Ph.D. degree in electrical engineering with the College of Electrical Engineering, Zhejiang University, Hangzhou, China.

Her research interests include electrical machines, servo motor drives, and power electronics.

Yanfei Cao (Member, IEEE) was born in Hebei, China, in 1990. She received the B.S. degree in automation from the Hebei University of Technology, City College, Tianjin, China, in 2013 and the M.S. and Ph.D. degrees in control science and engineering from Tianjin University, Tianjin, China, in 2015 and 2019, respectively.

She is currently an Associate Researcher with the College of Electrical Engineering, Zhejiang University, Hangzhou, China. Her research interests include electrical machines, motor drives, and power electronics.

Chen Li was born in Shandong, China, in 1991. He received the B.S. degree in electrical engineering from the China University of Mining and Technology, Jiangsu, China, in 2014, and the Ph.D. degree in electrical engineering from Tianjin University, Tianjin, China, in 2022.

He is currently a Postdoctoral Researcher with the Zhejiang University Advanced Electrical Equipment Innovation Center, Hangzhou, China. His current research interests include electrical machines, motor drives, and power electronics.

Zhiqiang Wang (Member, IEEE) was born in Tianjin, China, in 1984. He received the B.S. degree from the Hebei University of Technology, Tianjin, China, in 2006 and the M.S. and Ph.D. degrees from Tianjin University, Tianjin, China, in 2008 and 2012, respectively, all in electrical engineering.

He is currently an Associate Professor with the School of Electrical Engineering, Tiangong University, Tianjin, China. His research interests include power electronics technology and intelligent control of motor systems.

Tingna Shi (Senior Member, IEEE) was born in Yuyao, China, in 1969. She received the B.S. and M.S. degrees from Zhejiang University, Hangzhou, China, in 1991 and 1996, respectively, and the Ph.D. degree from Tianjin University, Tianjin, China, in 2009, all in electrical engineering.

She is currently a Professor with the College of Electrical Engineering, Zhejiang University, Hangzhou, China. Her current research interests include electrical machines and their control systems, power electronics, and electric drives.

Changliang Xia (Senior Member, IEEE) was born in Tianjin, China, in 1968. He received the B.S. degree from Tianjin University, Tianjin, China, in 1990, and the M.S. and Ph.D. degrees from Zhejiang University, Hangzhou, China, in 1993 and 1995, respectively, all in electrical engineering.

He was elected as an Academician of the Chinese Academy of Engineering, Beijing, China, in 2017. He is currently the President and a Full Professor of Tiangong University, Tianjin, China. He also serves as the Qiushi Chair Professor of Zhejiang University. His fields of research interests include electrical machines, power electronics, and their control systems.